Chapter 6

Two-Dimensional Analysis of Weak Shock Diffraction and Reflection in Extended Chaplygin Gas

6.1 Introduction

The study of shock waves, i.e., sudden, intense disturbances that propagate through a medium, has fascinated scientists and engineers for decades. These waves are not of just theoretical curiosities, they play a crucial role in many real-world applications, such as supersonic flight, explosion dynamics, and even astrophysical phenomena like supernovae. When a shock wave encounters a solid obstacle, such as a wedge, it can reflect, diffract, or even create complex patterns of waves. Understanding these interactions is essential for designing safer aircraft, predicting the effects of explosions, and modeling cosmic events.

In this chapter, our interest is in predicting the nature of waves when a shock hits, particularly near the corner of the wedge. Due to the impact of a weak shock, which is incident on the wedge, the reflection-diffraction phenomenon occurs. Here, we focus on a specific type of gas known as the extended Chaplygin gas (ECG), which behaves differently from the "ideal" gases typically studied in textbooks. Ideal gases follow simple rules, like the relationship between pressure and volume described by Boyle's law. However, in many real-world situations, especially under extreme conditions like high pressure or temperature, gases do not behave ideally. The ECG model provides a more accurate description of such gases by incorporating additional parameters that account for non-linear effects. The equation of state for this gas is given in equation (5.2.2).

For a better understanding of several Chaplygin gas models, see [14–17]. The equation (5.2.2) allows us to model gases that exhibit complex behaviour, such as those found in high-energy environments or in cosmological settings, where traditional ideal gas laws fall short. The ECG model is not just a theoretical construct, it has practical applications in several fields. In cosmology, for example, it is used to model dark energy and dark matter, i.e., mysterious substances that make up most of the universe but cannot be directly observed. The model's ability to describe exotic fluids with unusual pressure-density relationships makes it a valuable tool for understanding the universe's large-scale structure. In fluid dynamics, the ECG model helps researchers study shock waves in high-pressure and high-temperature environments, such as those encountered in supersonic flight or during explosions. By studying shock waves in ECG, we hope to shed light on the complex interactions that occur in high-energy environments, from the Earth's atmosphere to the far reaches of the cosmos. This research not only advances our understanding of fluid dynamics but also has practical applications in engineering, astrophysics, and beyond.

Much work has been carried out on characterizing the regular and Mach reflection configurations when the incident shock reflects off the wedge in gas dynamics [2, 66–69]. Most studies that have been carried out in [72, 73, 135, 136] deal with the reflection-diffraction phenomenon in an ideal gas. The significant studies done to show real gas effects on the reflection-diffraction phenomenon are presented in [81, 83].

The linear solution for the shock reflection-diffraction problem in isentropic gas was presented in [72], and later, the solution was modified using nonlinear geometric acoustic theory in [73]. The study presented in this chapter is influenced by the work done in [72, 73, 83]. This chapter considers the mathematical problem of shock hitting the right-angle wedge [73].

The chapter is organized as follows. Section 6.2 introduces the fundamental equations of gas dynamics that describe the reflection-diffraction phenomenon in the context of an extended Chaplygin gas, along with the relevant boundary conditions. Section 6.3 elaborates on the Rankine-Hugoniot (R-H) conditions, which are used to derive the asymptotic expressions for the state variables in regions $(\bar{1})$ and $(\bar{2})$, as shown in Fig. 6.1. Section 6.4 examines the behaviour of these asymptotic expansions within the diffracted region. A singularity is identified near the boundary of the diffracted region, and Section 6.5 provides a detailed analysis of the nonlinear expansion of solutions in the vicinity of this singularity. Section 6.6 explores the behaviour of nonlinear expansions near the singular point in greater detail. The numerical results and discussions are presented in Section 6.7. Finally, Section 6.8 summarizes the key findings and conclusions of the study.

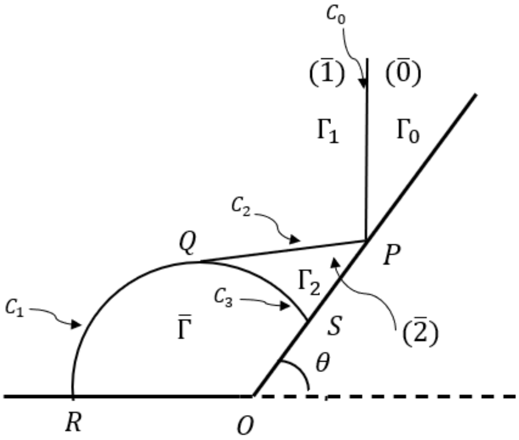

Figure 6.1: Incident shock C_0 hits the wedge inclined at angle θ at point P. The reflection-diffraction phenomena in a self-similar plane (ξ, η). C_1: diffracted shock, C_2: reflected shock, C_3: rarefaction wave.

6.2 Fundamental equations and Configuration of shock reflection-diffraction in self-similar flow

This section begins by formulating the compressible, isentropic Euler system with specialized boundary conditions describing the reflection-diffraction phenomenon. A change of variables transforms the transient governing laws into a steady-state problem in a self-similar flow. We then identify and label the subregions occupied by the reflected and diffracted disturbances in that self-similar plane.

The governing equations and equation of state are similar to the equations given in (5.2.1) and (5.2.2).

When a weak shock strikes the wedge inclined at angle $\theta \in (0, \pi/2)$ in (X, Y, t) - space as shown in Fig. 6.1, a reflection-diffraction phenomenon occurs. In Fig. 6.1, a planar shock C_0 hits the rigid wedge at $t = 0$. We represent the states ahead and behind the incident shock by $(\bar{0})$ and $(\bar{1})$ and the variables (ρ, U, V, a) are considered to be $(\rho_0, 0, 0, a_0)$ and $(\rho_1, U_1, 0, a_1)$, respectively. In variables (ρ, U, V, a), a represents the speed of sound and is given by $a = \sqrt{\partial p / \partial \rho}$. Moreover, the initial conditions at $t = 0$ may be written as

$$(\rho, U, V, a) = \begin{cases} (\rho_0, 0, 0, a_0), & X > 0,\ Y > X \tan\theta \\ (\rho_1, U_1, 0, a_1), & X < 0, \end{cases} \tag{6.2.1}$$

And the boundary condition along the wedge is given by

$$V = U \tan\theta, \quad X > 0,\ t > 0. \tag{6.2.2}$$

The system of Euler equations (5.2.1) may be transformed into the self-similar plane using the pseudo-variables $\xi = \sqrt{(X^2 + Y^2)}/t$ and $\eta = \arctan(Y/X)$ [84]. The transformed system of equations in the self-similar plane is given by as that of equation (5.2.5). The velocity components u and v may be represented as (5.2.6). The initial and boundary conditions in self-similar flow are obtained by using equation (5.2.6) in equation (6.2.1) and are given by

$$\lim_{\xi \to \infty} (\rho, u, v, a) = \begin{cases} (\rho_0, 0, 0, a_0), & \theta < \eta < \frac{\pi}{2} \\ (\rho_1, U_1 \cos\eta, -U_1 \sin\eta, a_1), & \frac{\pi}{2} < \eta < \quad , \\ pi \end{cases} \tag{6.2.3}$$

and at $\eta = \theta$, the condition is similar to the condition given in equation (5.2.8) respectively. Here, $a_0 = \sqrt{\mathcal{A}}\rho_0^{(n-1)/2}(n(1-b')^{(-n-1)} + \alpha B')^{1/2}$, $b' = b\rho_0$ and $B' = \mathcal{B}/(\mathcal{A}\rho_0^{\alpha+n})$. In this case also, the matrix form of system (5.2.5) may be given as (5.2.9).

We assume that a planar shock hits the rigid wedge at P at time $t = 0$ (see Fig. 6.1), and at $t > 0$, it starts propagating along the rigid wedge. When an incident shock hits the wedge, according to linear acoustics [72], a part of the incident planar shock is reflected, and another part is diffracted within a circle of radius $r = a_0 t$ centered at the corner O of the rigid wedge shown in Fig. 6.1. In Fig. 6.1, the curved portions PQ and QR represent the reflected and diffracted shocks, respectively [73]. The curved part QS denotes the rarefaction. The position of the incident shock far away from the corner O of the wedge is given as similar to (5.2.10) and that of reflected shock is

$$\xi^* = a_0 \tan\theta / (\sin(\eta - \theta)\sec\theta + \sin(2\theta - \eta)). \tag{6.2.4}$$

The domain Γ of the entire flow is divided into four regions $\Gamma_0, \Gamma_1, \Gamma_2$ and $\bar{\Gamma}$ by the reflection-diffraction phenomenon of planar incident shock and depicted in Fig. 6.1. The region $\overline{\Gamma}$ is called the diffracted region. The entire region of flow in the self-similar plane is given by

$$\Gamma = \Gamma_0 \cup \Gamma_1 \cup \Gamma_2 \cup \overline{\Gamma},$$

where

$$\begin{aligned}
&\Gamma_0 = \{(\xi,\eta)|\ \xi > a_0 \sec\eta, \theta < \eta < \frac{\pi}{2}\},\\
&\Gamma_1 = \{(\xi,\eta)|\ \xi^* < \xi < a_0 \sec\eta, \theta < \eta < 2\theta\} \cup \{(\xi,\eta)|\xi > a_0, 2\theta < \eta < \pi\},\\
&\Gamma_2 = \{(\xi,\eta)|\ \xi^* > \xi > a_0, \theta < \eta < 2\theta\},\\
&\overline{\Gamma} = \{(\xi,\eta)|\ \xi < a_0, \theta < \eta < \pi\}.
\end{aligned}$$

In Fig. 6.1, *C_0* is the incident shock, which hits the wedge at P. In this context, the segment QS serves as the sonic curve, defined by $\xi = a_0$, where a smooth transition occurs from the supersonic region Γ_2 to the subsonic region $\overline{\Gamma}$. In contrast, QR is the free boundary associated with the diffraction of the planar shock, across which the flow abruptly shifts from the supersonic region Γ_1 to $\overline{\Gamma}$ near the origin. While the flow remains constant in regions Γ_1 and Γ_2, it exhibits a pseudo-subsonic behaviour in $\overline{\Gamma}$.

The hyperbolic Euler system (5.2.1) dictates the overall flow pattern. However, when expressed in self-similar coordinates (ξ, η), the flow is described by mixed-type equations (5.2.9), which transition from elliptic to hyperbolic as the point (ξ, η) moves from the origin toward infinity. Consequently, one must solve the free boundary value problem for a degenerate elliptic equation to accurately determine the entire flow field and its associated wave structure.

6.3 R-H conditions for the incident and reflected shock and asymptotic expansions

This section describes the R-H conditions to find the states ahead and behind the reflected shock. Moreover, asymptotic expansions are presented for both states.

The RH-conditions may be considered similar to (5.3.1) and their representation in self-similar plane is given by (5.3.2). The asymptotic expansions of variables of state - $(\overline{1})$ may be found in (5.3.5). Making use of equation (5.3.3) - (5.3.5) in (5.3.2), the unknowns of the asymptotic expansions of ρ_1/ρ_0, u_1/σ_0, v_1/σ_0, a_1/σ_0 and ξ/σ_0 in (5.3.5) of state - $(\overline{1})$ are obtained and given by as that of in (5.3.5).

To obtain the variables of state - $(\overline{2})$, the asymptotic expansions for ρ_2/ρ_0, u_2/σ_0, v_2/σ_0 are given in $(5.3.6)_1$ - $(5.3.6)_3$ and of ξ^*/σ_0 is given by

$$\frac{\xi^*}{\sigma_0} = K_0 \tan\theta/(\sin(\eta-\theta)\sec\theta + \sin(2\theta-\eta)) + \mathcal{O}(\delta), \tag{6.3.1}$$

To find the values of ρ_2, u_2, and v_2, equations (5.3.5), $(5.3.6)_1$ - $(5.3.6)_3$ and (6.3.1) are used in R-H conditions in self-similar flow (5.3.2) and are found as;

$$\begin{aligned}
&\rho_1^{(2)} = 2, \;\; u_2^{(1)} = 2K_0 \cos\theta \cos(\eta - \theta),\\
&u_2^{(2)} = K_0 \cos(\eta - \theta)\Bigg[2\cot^2\theta\cos\theta\\
&+ (\cot\theta\csc\theta + \cos\theta)\frac{n(n-3+4b') - \alpha(\alpha+3)B'(1-b')^{n+2}}{4(1-b')(n+\alpha B'(1-b')^{n+1}}\Bigg]\\
&v_2^{(1)} = -K_0 \cos\theta \sin(\eta - \theta),\\
&v_2^{(2)} = -K_0 \cos(\eta - \theta)\Bigg[2\cot^2\theta\cos\theta\\
&+ (\cot\theta\csc\theta + \cos\theta)\frac{n(n-3+4b') - \alpha(\alpha+3)B'(1-b')^{n+2}}{4(1-b')(n+\alpha B'(1-b')^{n+1}}\Bigg].
\end{aligned}$$

Note that, while solving equations (5.3.2), coefficients of δ in orders 1 and 2 are compared. From equations $(5.3.5)_1$ and $(5.3.6)_1$, it is seen that the first-order approximation of the variable ρ is given by

$$\rho_1^{(i)}(\xi,\eta) = \begin{cases} 1, & (\xi,\eta) \in \Gamma_1 \\ 2, & (\xi,\eta) \in \Gamma_2 \end{cases}, \quad i = 1, 2. \tag{6.3.2}$$

In equation (6.3.2), $\rho_1^{(i)}(\xi,\eta)$ is piecewise constant in the region $\Gamma \setminus \bar{\Gamma}$.

6.4 Asymptotic expansions in the diffracted region $\bar{\Gamma}$

In this section, the asymptotic behaviour of the solution in the diffracted region is analyzed. To obtain the approximate solution in the diffracted region, a dimensionless parameter $\bar{\xi} = \xi/a_0$ is introduced, and the asymptotic expansions of variables

(ρ, u, v) are considered as (5.4.1). Similar analysis is done as in Section 5.4, for equations (5.4.2)-(5.4.4) and the solution of Laplace equation (5.4.4) may be found as

$$\overline{\rho_1} = 1 + \frac{1}{\pi} \arctan\left(\frac{\sqrt{3}\left(1 - \overline{r}^{\pi/(\pi-\theta)} \cos\frac{\pi^2}{2(\pi-\theta)}\right)}{\left(1 + \overline{r}^{\pi/(\pi-\theta)}\right) \sin\frac{\pi^2}{2(\pi-\theta)} + 2\overline{r}^{\pi/(\pi-\theta)} \cos\left(\frac{(\eta-\theta)\pi}{2(\pi-\theta)}\right)}\right). \tag{6.4.1}$$

From equation (6.4.1), it may be observed that if $\overline{\rho_1}$ does not exist at $\overline{r} = 1$ or at $\overline{\xi}$=1. Therefore, $\overline{\xi} = 1$ or $\xi = a_0$ is the point of singularity. The solution $\overline{\rho_1}$ is invalid in the whole region $\overline{\Gamma}$. As one moves along the boundary, C_1 i.e., along the diffracted wavefront, the normal derivative of the linear solution, $\overline{\rho_1}$ i.e., $\overline{\rho_1}_{\overline{r}}$ is unbounded, whereas both the normal and tangential derivatives $\overline{\rho_1}_{\overline{r}}$ and $\overline{\rho_1}_{\eta}$, respectively, are unbounded at the triple point Q, which forces one to include the non-linear effects at those points where the singularity occurs. For equation of state (5.2.2), the singularity is found at $\overline{\xi} = 1$ or $\xi = a_0$. To find the nonlinearity effect near $\overline{\xi} = 1$, following expansion of equation (6.4.1) may be considered for $j = 1, 2$ as

$$\overline{\rho_1} = \rho_1^{(j)} + \frac{\sqrt{2}}{\pi} \frac{\frac{\pi}{2(\pi-\theta)} \sin\frac{\pi^2}{2(\pi-\theta)}}{\cos^2\frac{\pi(\eta-\theta)}{2(\pi-\theta)} - \sin\frac{\pi^2}{2(\pi-\theta)}} \left(1 - \overline{\xi}\right)^{1/2} + \mathcal{O}\left(1 - \overline{\xi}\right) + \mathcal{O}\left(\frac{\delta^2}{(1-\overline{\xi})^{1/2}}\right), \tag{6.4.2}$$

Therefore, from equations (5.4.1) and (6.4.2), the expression of ρ is given by

$$\frac{\rho}{\rho_0} = 1 + \rho_1^{(j)}\delta + \frac{\sqrt{2}}{\pi} \frac{\frac{\pi}{2(\pi-\theta)} \sin\frac{\pi^2}{2(\pi-\theta)}}{\cos^2\frac{\pi(\eta-\theta)}{2(\pi-\theta)} - \sin\frac{\pi^2}{2(\pi-\theta)}} \left(1 - \frac{\xi}{a_0}\right)^{1/2} + \delta\mathcal{O}\left(1 - \frac{\xi}{a_0}\right) + \delta^2\mathcal{O}\left(\left(1 - \frac{\xi}{a_0}\right)^{-1/2}\right). \tag{6.4.3}$$

6.5 Nonlinear expansions on curve RQS

In this section, nonlinear approximations are considered to analyze the effect of singularity on diffraction-reflection phenomena. Nonlinear approximations play a significant role in the solution near the point of singularity. It may be observed in equation (6.4.1) that the singularity is found at $\xi = a_0$. It may be noticed that the system of equations (5.2.9) shows degeneracy at point $\xi = u_0 + a_0, u_0, u_0 - a_0$ i.e. $\xi = a_0, 0, -a_0$. In order to study the nonlinear effect, $\xi = a_0$ the expression of ξ near a_0 may be taken as (5.5.1).

For $\xi = a_0$ and $\eta (\neq 2\theta)$, arc RQS may be divided into two parts C_1 and C_3, which represent the diffracted shock and expansion wave, respectively, as shown in Fig. 6.1. The expansions on the boundaries C_1, and C_3 may be expressed as (5.5.3).

Following the similar analysis as done in Section 5.5 in Chapter 5, equations (5.5.4) - (5.5.15) may be obtained.

On comparison of equations (6.4.3) and (5.5.15), it is obtained that for $\delta << 1 - \frac{\xi}{a_0} << 1$,

$$\frac{\sqrt{2}}{\pi} \frac{\frac{\pi}{2(\pi-\theta)} \sin \frac{\pi^2}{2(\pi-\theta)}}{\cos^2 \frac{\pi(\eta-\theta)}{2(\pi-\theta)} - \sin \frac{\pi^2}{2(\pi-\theta)}} = \begin{cases} \left(\frac{-a_0}{I_0(\eta)}\right)^{1/2}, & \eta < 2\theta \\ -\left(\frac{-a_0}{I_0(\eta)}\right)^{1/2}, & 2\theta < \eta < \pi \end{cases} \tag{6.5.1}$$

From equation (6.5.1), it may be noticed that $1/I_0(\eta)$ exists for all values of $\eta(\neq 2\theta)$ and is given by

$$\frac{1}{I_0(\eta)} = -\frac{2}{a_0} \left\{ \frac{\frac{\pi}{(\pi-\theta)} \sin \frac{\pi^2}{(\pi-\theta)}}{\pi(\cos^2 \frac{\pi(\eta-\theta)}{2(\pi-\theta)} - \sin \frac{\pi^2}{2(\pi-\theta)})} \right\}^2 . \tag{6.5.2}$$

From equation (5.5.12) and (6.5.2), the location of diffracted shock for $\eta(\neq \pi)$ is given by

$$\omega_s = \mathcal{C} + \frac{1}{8}\frac{3\sigma_0\left(\frac{\pi}{\pi-\theta}\right)^2 \sin^2\frac{\pi^2}{(\pi-\theta)}}{\pi^2\left(\cos^2\frac{\pi(\eta-\theta)}{2(\pi-\theta)} - \sin\frac{\pi^2}{2(\pi-\theta)}\right)^2}\left\{\frac{n(n-1+2b') + \alpha B'(1-b')^{n+2}}{(1-b')(n+\alpha B'(1-b')^{n+1})}\right\}^2 . \tag{6.5.3}$$

Solution of partial differential equation (5.4.3) with boundary condition (5.5.7), may be obtained with the help of equations (5.5.8) and (6.5.3) and may be considered for $2\theta < \eta < \pi$ and $\theta < \eta < 2\theta$ separately.

(i) When $2\theta < \eta < \pi$, the wavefront represents a shock wave, and the jump is given by eq (5.5.19).

(ii) When $\theta < \eta < 2\theta$, the wavefront represents a rarefaction wave, and the jump is given by eq (5.5.20).

It may be noticed that the jumps presented in equations (5.5.19) and (5.5.20) show the strengths of the shock wave and rarefaction wave, respectively, and are shown by QR and QS in Fig. 6.1. Positive and negative roots in equations (5.5.19) and (5.5.20) show an increase in density across the shock and a decrease in the rarefaction wave, respectively.

6.6 Nonlinear expansions near singular point Q

It may be observed that the expansions derived in Section 6.5 to represent the solution near the diffracted front are not valid near the singular point since the shock strength and position ω are found to approach infinity when one moves close to point

Q. This section presents an expansion to obtain the solution in the neighborhood of the singular point.

In order to present an expansion near a singular point Q in Fig. 6.1, new variables are introduced as given in equation (5.7.1) and a similar analysis is done and the similar nonlinear behaviour is observed near point Q.

6.7 Numerical Results and Discussion

Diffracted shock, expansion wave profiles, as well as the shock position, are explained in this section for various values of the considered parameters. In Section 6.7.1, the behaviour of diffracted shock and expansion wave profiles is plotted. Further, the shock speed is discussed in Section 6.7.2.

6.7.1 Diffraction Shock and Expansion wave Profile

In this section, we present the shock wave solutions within the $(\tilde{\rho}, \omega)$-plane. The shock wave profile, as defined by equation (5.5.8), is depicted in Fig. 6.2 using the relationships specified in equations (6.5.2) and (5.5.12). The parameters utilized for this analysis are $n = 1.4$, $B' = 0.5$, $\alpha = 0.5$, $\theta = \pi/6$. The solid line segments $h_1s_1 \cup g_1h_3$ and $h_2s_2 \cup g_2h_3$ depict the shock wave profiles for $b' = 0.3$ and $b' = 0.4$, respectively. In each case, the dashed segment (s_1g_1 for $b' = 0.3$ and s_2g_2 for $b' = 0.4$) highlights the discontinuity in the profile, with g_1 and g_2 denoting the positions of the shocks.

For $\omega < \omega_s$, the solution ρ traces the upper half of the parabolic curve. At $\omega = \omega_s$, the shock is situated, and for $\omega > \omega_s$, the boundary condition $\tilde{\rho} = \rho_i^{(2)}$ holds.

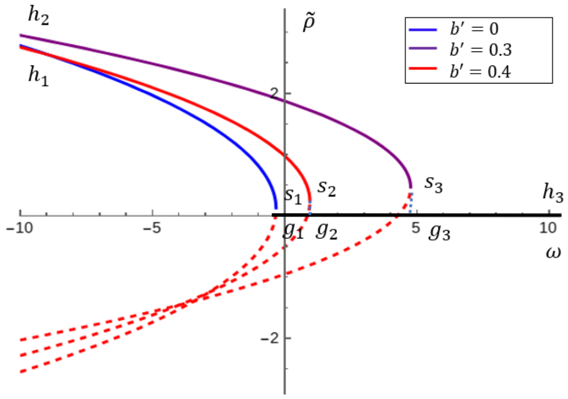

FIGURE 6.2: Plots of diffracted shock wave profile equation (5.5.8) with $n = 1.4, B' = 0.5, \alpha = 0.5, \eta = 2\pi/3, \theta = \pi/6$, $\rho_i^{(2)} = 0$. Solid lines $h_1s_1 \cup g_1h_3$, $h_1s_2 \cup g_2h_3$ and $h_2s_3 \cup g_3h_3$ represent shock wave profiles for $b' = 0, 0.3$ and $b' = 0.4$, respectively. s_1g_1, s_2g_2 and s_3g_3 are jumps in shock profiles. g_1, g_3 and g_3 represent shock positions.

Notably, altering b' affects both the shock's position and the magnitude of the jump in $\tilde{\rho}$, indicating a change in the shock's strength.

Figs. 6.3(a) and 6.3(b) illustrate the shock wave solutions for two distinct parameter sets: Fig. 6.3(a) presents results for $B' = 0.1$ and $B' = 0.6$, while Fig. 6.3(b) displays solutions for $\alpha = 0.1$ and $\alpha = 1.0$. Although variations in B' and α influence the

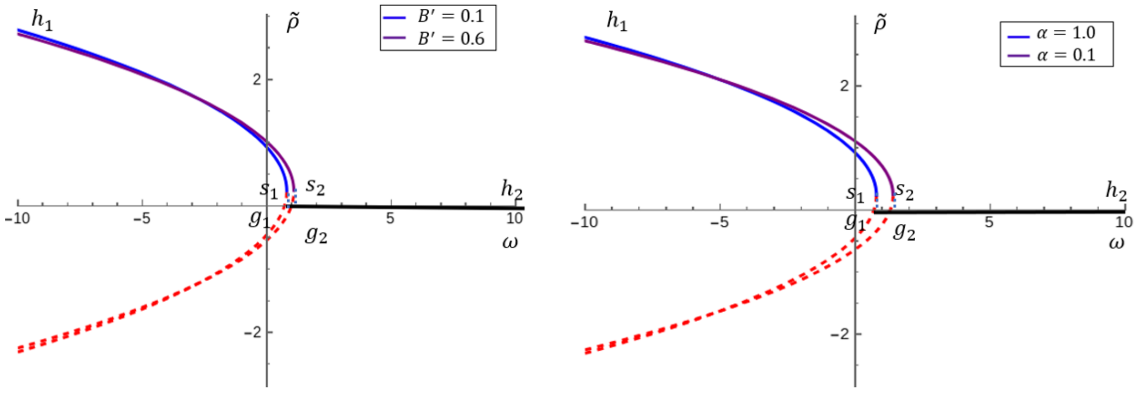

(a) (b)

FIGURE 6.3: Plots of diffracted shock wave profile equation (5.5.8) with (a) $n = 1.4, b' = 0.2, \alpha = 0.5, \eta = 2\pi/3, \theta = \pi/6$ (b) $n = 1.4, b' = 0.2, B' = 0.6, \eta = 2\pi/3, \theta = \pi/6$.

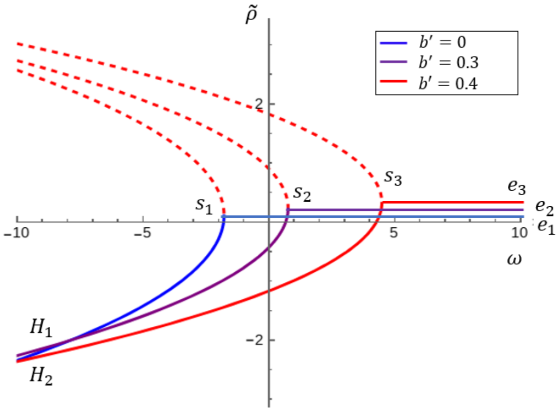

FIGURE 6.4: Plots of expansion Wave profile, $\tilde{\rho}$ vs. ω: equation (5.5.8) with $n = 1.4, B' = 0.5, \alpha = 0.5, \eta = \pi/4, \theta = \pi/6$, $\rho_i^{(2)} = 0$. Solid lines $H_1s_1e_1$, $H_2s_2e_2$ and $H_2s_3e_3$ represent expansion wave profiles for $b' = 0, 0.3$ and $b' = 0.4$, respectively.

shock positions, they do not affect the magnitude of the jump in $\tilde{\rho}$, indicating that the shock's strength remains unchanged.

Figs. 6.4 and 6.5 depict the expansion wave profiles within the self-similar plane, highlighting the influence of parameters b', B', and α. These profiles correspond to the lower branch of the parabola defined in equation (5.5.8).

In Fig. 6.4, the plot of $\tilde{\rho}$ versus ω is presented for the parameter set $n = 1.4$, $B' = 0.5$,

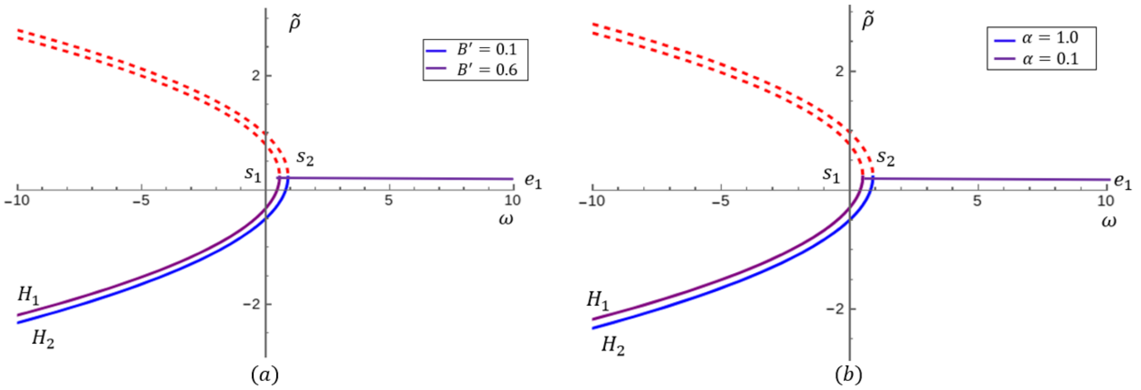

FIGURE 6.5: Plots of expansion Wave profile, $\tilde{\rho}$ vs. ω: equation (5.5.8) with (a) $n = 1.4, b' = 0.2, \alpha = 0.5, \eta = \pi/4, \theta = \pi/6$ (b) $n = 1.4, b' = 0.2, B' = 0.6, \eta = \pi/4, \theta = \pi/6$.

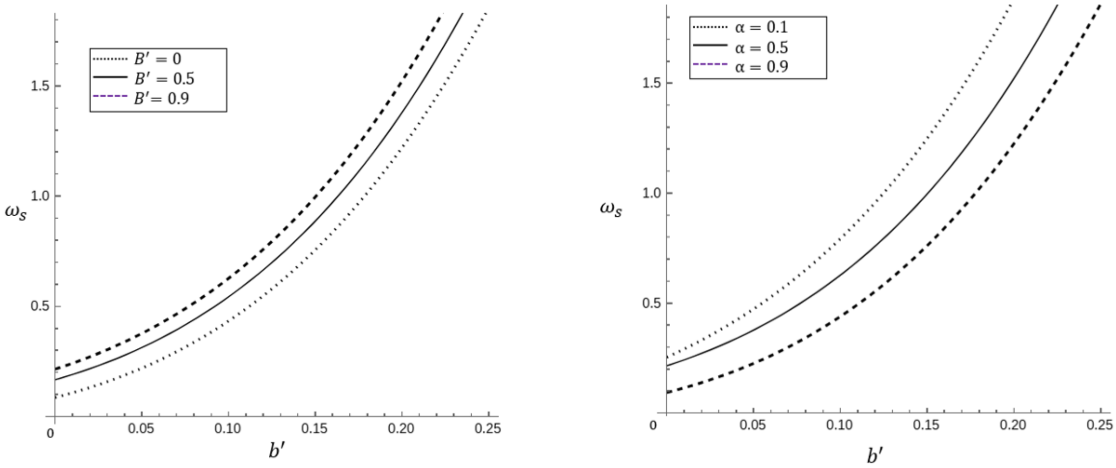

(a) (b)

FIGURE 6.6: Plots of speed of diffracted shock ω_s vs. b': equation (5.5.8) with (a) $n = 1.4, b' = 0.2, \alpha = 0.1, \eta = 2\pi/3, \theta = \pi/6$ (b) $n = 1.4, b' = 0.2, B' = 0.9, \eta = 2\pi/3, \theta = \pi/6$.

$\alpha = 0.5$, $\eta = \pi/4$, $\theta = \pi/6$, and $\rho_i^{(2)} = 0$, while varying b'. The solid lines labeled $H_1s_1e_1$, $H_2s_2e_2$, and $H_2s_3e_3$ represent the expansion wave profiles for $b' = 0$, 0.3, and 0.4, respectively.

Similarly, Fig. 6.5(a) displays the profiles $H_1s_1e_1$ and $H_2s_2e_1$ for $B' = 0.1$ and $B' = 0.6$, respectively. In Fig. 6.5(b), the expansion wave profiles $H_1s_1e_1$ and $H_2s_2e_1$ are shown for $\alpha = 1.0$ and $\alpha = 0.1$, respectively.

6.7.2 Shock Position or speed of the diffracted shock

In this section, we examine the shock location within the self-similar plane. The position of the diffracted shock, denoted as ω_s, is defined by equation (6.5.3), where ω_s represents the shock velocity in polar coordinates. We explore the relationship between the shock location (or velocity) and the parameter b' for various values of B' and α.

Figs. 6.6(a) and 6.6(b) illustrate how ω_s varies with b' for different values of B' and α. Specifically, Fig. 6.6(a) shows the variation of ω_s with b' for $B' = 0$, 0.5, 0.9, while Fig. 6.6(b) depicts the variation for $\alpha = 0.1$, 0.5, 0.9. Notably, Fig. 6.6(a) reveals that the shock speed in an ideal gas ($b' = B' = 0$) is slower compared to that in a non-ideal gas. Additionally, increasing the non-linearity parameter B' results in a higher shock velocity. Similarly, Fig. 6.6(b) demonstrates that the shock speed increases as the value of α rises.

6.8 Conclusions

Meticulous examination has been performed with the objective of unravelling the impact of extended Chaplygin gas on the flow configuration on various boundaries of the whole region when a weak shock reflects and diffracts off a wedge inclined at an arbitrary angle. By transforming the region into a self-similar plane and using the R-H conditions, the asymptotic expansions of the immediate state behind the incident and reflected shocks are obtained. The nonlinear expansions in the diffracted region, as well as on boundaries representing the diffracted shock and rarefaction, are obtained. Moreover, the nonlinear asymptotic expansion at the intersection Q of the diffracted shock, reflected shock, and expansion wave profiles boundaries. With the aid of finding the asymptotic expansions in various regions and boundaries, the effect of the nonideal gas parameters b and $\mathcal{B}$, and α is discussed for the shock and expansion wave profiles as well as for the shock speeds or shock positions. The graphical presentations of the considered parameter effects are shown. Some of the remarkable outcomes of the current study can be highlighted as:

- The nonideal parameter b alters both the shock position and the shock's strength, and both increase with the increase in b. Therefore, with an increase in the values of b, the boundary RQ becomes stronger in the extended Chaplygin gas than in the ideal gas.

- The shock positions vary with different values of $\mathcal{B}$ and α; the shock's strength seems to be less effective.

- Increase in the non-linearity parameter $\mathcal{B}$ results in a higher shock velocity. On the contrary, the shock speed decreases as the value of α increases.

- The rarefaction wave (expansion wave) is weakened while the diffracted shock is simultaneously strengthened by the extended Chaplygin gas effects.

****